

1     **Magnetosphere-Ionosphere-Thermosphere coupling at Jupiter**  
2     **using a three-dimensional atmospheric general circulation**  
3     **model**

4     **J. N. Yates<sup>1,2</sup>, L. C. Ray<sup>3</sup>, N. Achilleos<sup>4,5</sup>, O. Witasse<sup>6</sup>, and N. Altobelli<sup>1</sup>**

5                             <sup>1</sup>European Space Agency, ESAC, Spain

6                             <sup>2</sup>Imperial College London, UK

7                             <sup>3</sup>Lancaster University, UK

8                             <sup>4</sup>University College London, UK

9                             <sup>5</sup>Centre for Planetary Science, UCL-Birkbeck, UK

10                            <sup>6</sup>European Space Agency, ESTEC, Netherlands

11     **Key Points:**

- 12     • A new model of Jupiter's magnetosphere-ionosphere-thermosphere coupling is pre-  
13     sented.  
14     • This new 3D model demonstrates the importance of including zonal terms in the  
15     momentum and energy equations.  
16     • The high-latitude temperatures are comparable to the lower range of observed tem-  
17     peratures.

---

Corresponding author: J.N. Yates, [japheth.yates@esa.int](mailto:japheth.yates@esa.int)

## Abstract

Jupiter's upper atmosphere is  $\sim 700$  K hotter than predicted based on solar extreme ultraviolet heating alone. The reason for this still remains a mystery and is known as the 'energy crisis'. It is thought that the interaction between Jupiter and its dynamic magnetosphere plays a vital role in heating its atmosphere to the observed temperatures. Here, we present a new model of Jupiter's MIT coupled system where we couple a three-dimensional atmospheric general circulation model to an axisymmetric magnetosphere model. We find that the model temperatures are on average  $\sim 60$  K, with a maximum of  $\sim 200$  K, hotter than the model's two-dimensional predecessor making our high-latitude temperatures comparable to the lower limit of observations. Stronger meridional winds now transport more heat from the auroral region to the equator increasing the equatorial temperatures. However, despite this increase, the modelled equatorial temperatures are still 100s of Kelvin colder than observed. We use this model as an intermediate step towards a three-dimensional atmospheric model coupled to a realistic magnetosphere model with zonal and radial variation.

## 1 Introduction

The solar system's giant planets all have very hot upper atmospheres. Their atmospheres are much hotter than would be expected if they were heated primarily by solar extreme ultraviolet radiation (EUV) like the terrestrial upper atmosphere. Jupiter's thermosphere is  $\sim 700$  K ( $\sim 4.5\times$ ) hotter than predicted [e.g. *Strobel and Smith*, 1973; *Seiff et al.*, 1998; *Yelle and Miller*, 2004]. The other giant planets Saturn, Uranus, and Neptune are respectively  $\sim 2.5\times$ ,  $\sim 5.8\times$ , and  $\sim 4.5\times$  hotter than predicted. This is known as the giant planet energy crisis. To date, we still cannot explain the source of these high temperatures despite many attempts. The high thermospheric temperatures at Jupiter are thought to be caused by i) the interaction between its upper atmosphere and magnetosphere via Joule heating [*Waite et al.*, 1983; *Millward et al.*, 2005; *Smith et al.*, 2005], ion drag [*Miller et al.*, 2000; *Millward et al.*, 2005; *Smith et al.*, 2005] and particle precipitation – be it auroral [*Waite et al.*, 1983; *Grodent et al.*, 2001] or mid- and low-latitude [*Yelle and Miller*, 2004]; ii) the breaking of acoustic and/or gravity waves in the upper atmosphere [*Young et al.*, 1997; *Matcheva and Strobel*, 1999; *Hickey et al.*, 2000; *Schubert et al.*, 2003]; or iii) by some combination of both. The Galileo probe's descent into Jupiter's atmosphere remains the only potential in situ evidence of Jovian atmospheric waves [*Young et al.*, 1997]. Combined with the fact that such waves are difficult to detect remotely it is complicated to quantify and confirm the plethora of waves and wave modes that can be sustained within Jupiter's atmosphere. Recently, *Müller-Wodarg et al.* [2019] discovered atmospheric waves present in Saturn's thermosphere. The authors found that these waves may be damped and as such could enhance the eddy friction resulting in an increase in atmospheric temperature. Due to the similarity between Jupiter and Saturn such damped waves could also be present in the Jovian system and should be considered in future studies. In this study, we therefore focus solely on the magnetospheric interaction.

The interaction between a planet's upper atmosphere, consisting of an ionosphere embedded in a neutral thermosphere, and magnetosphere is known as magnetosphere-ionosphere-thermosphere (MIT) coupling. This coupled system is investigated using numerical models, where the neutral atmosphere is represented by a general circulation model (GCM) which is coupled to either a simplified model representing the currents in the magnetosphere-ionosphere (MI) system [*Smith and Aylward*, 2009; *Tao et al.*, 2009, 2010, 2014; *Ray et al.*, 2015; *Yates et al.*, 2012, 2014; *Yates et al.*, 2018] or by imposing electric fields directly into the thermospheric GCM [*Achilleos et al.*, 1998, 2001; *Bougher et al.*, 2005; *Majeed et al.*, 2005, 2009, 2016; *Millward et al.*, 2002, 2005]. The Jovian Ionosphere Model (JIM) (*Achilleos and Millward*) and the Jupiter Thermospheric GCM (JT-GCM) (*Bougher and Majeed*) are models which investigated the 3D dynamics and chem-

istry of Jupiter’s upper atmosphere and its MIT coupling. The JIM model was the first Jovian 3D MIT coupling model employing an offset tilted dipole magnetic field model and an Earth-like parameterization of Jupiter’s ionospheric electric field. JIM investigated the creation of Jupiter’s ionosphere within the auroral region and how ionospheric ion motion influenced the thermospheric neutrals. JTGCM simulates MIT coupling by using terrestrial parameterizations of ion drag and Joule heating and ion drifts generated using a convection electric field model based on Voyager measurements. Joule heating is then scaled down until the model reproduces the observed temperatures. Both JIM and JTGCM model how the neutral winds are modified by their coupling with Jupiter’s ionospheric ions and the resulting re-distribution of heat from the auroral regions to lower latitudes. The resulting neutral flows amount to a sub-corotational (westward) zonal jet at high-latitudes, equatorward high-altitude flows and poleward flows in the high-latitude and low-altitude thermosphere. JTGCM’s flows are, however, very asymmetric in coverage and speeds due to their use of the VIP4 [Connerney *et al.*, 1998] magnetic field model instead of a simple tilted-dipole field, and some may argue that this is more realistic.

The 3D models presented above impose magnetospheric forcing in the polar regions but do not self-consistently couple the magnetosphere to the upper atmosphere. Self-consistently coupling the magnetosphere and ionosphere-thermosphere allows the field-aligned currents to affect the magnetospheric convection electric field and magnetospheric plasma. A series of models were subsequently developed to self-consistently include such coupling. Due to the complexity of such coupling the models were designed to initially be axisymmetric. The *Smith and Aylward* [2009]; *Tao et al.* [2009]; *Ray et al.* [2015] and *Yates et al.* [2014] models all consist of a one-dimensional (1D) magnetosphere model self-consistently coupled to a two-dimensional (2D) atmospheric GCM. Of all the 2D coupled MIT models, only the *Tao et al.*, models could reproduce atmospheric temperatures comparable to those observed at all latitudes by including heating terms due to acoustic waves as parameterized by *Schubert et al.* [2003]. The other 2D models did not include heating due to acoustic wave breaking for reasons given above. This means that their temperatures, particularly at equatorial latitudes, were modelled to be much lower ( $\sim 300$  K) than observed ( $\sim 900$  K). It is worth noting that the *Smith et al.*, model can reproduce the observed temperatures if the authors include an extra, low-latitude, Joule heating term due to fluctuating electric fields. Regarding neutral dynamics, the suite of 2D models found similar flow cells to those found using the 3D models albeit with generally lower meridional velocities. Most MIT coupling studies assume that the system is in quasi-equilibrium (or steady state). The works of *Yates et al.* [2014]; *Tao et al.* [2014]; *Yates et al.* [2018] were the first to include time-dependence outside of the thermospheric GCM by either having a time-dependent magnetospheric size [*Yates et al.*, 2014; *Yates et al.*, 2018] or solar EUV flux [*Tao et al.*, 2014]. Including variable solar EUV fluxes (factors of one to three) results in moderate thermospheric temperature ( $\sim 10$  K) and neutral velocity ( $\sim 20\%$ ) increases while large changes in magnetospheric size ( $\sim 40 R_J$ ; Jovian radii with  $1 R_J = 71492$  km) lead to temperature variations of a few tens of Kelvin. Moreover, varying the size of the magnetosphere leads to an increase in equatorward transport of heat which is typically prohibited in the steady-state simulations pertaining to Jupiter and Saturn [e.g. *Smith and Aylward*, 2008, 2009]. If we exclude the effect of wave heating, the time-dependent additions discussed above have been unable to reproduce the observed temperatures despite adding considerable complexity to the MIT coupling models.

This study presents results from a newly developed Jovian 3D thermospheric GCM self-consistently coupled to a 1D magnetosphere model. We describe our coupled model including its limitations in section 2 and present our simulation results while comparing them to its 2D progenitor model [*Yates et al.*, 2014] in section 3. In section 4 we discuss how the new model compares to available observations and previous Jovian 3D models. We summarize and conclude in section 5.

## 2 Model description

The coupled magnetosphere-ionosphere-thermosphere steady-state model presented here is largely based on that presented in numerous studies [e.g. *Smith and Aylward*, 2009; *Yates et al.*, 2014; *Ray et al.*, 2015] and as such we will briefly summarize the model below and introduce the new components that have been added for this study.

### 2.1 Thermosphere model

The thermosphere model here is a GCM solving the full time-dependent non-linear three-dimensional (3D) Navier-Stokes equations of energy, momentum and continuity, using explicit time integration [*Müller-Wodarg et al.*, 2006] and a time-step of 3s. The model has been developed from the 2.5D (2.5D because zonal gradients in the Navier-Stokes equations are not included) azimuthally symmetric GCM of *Smith and Aylward* [2009] to fully include the third dimension. Our new model solves the Navier-Stokes equations in a spherical-pressure coordinate system, providing time dependent distributions of thermospheric wind, temperature and energy. The horizontal (zonal and meridional) momentum, energy and continuity equations which we solve can be found in *Achilleos et al.* [1998] or *Müller-Wodarg et al.* [2006]. We assume hydrostatic equilibrium in our model so the full vertical momentum equation is not solved. Our model is resolved on a  $0.2^\circ$  latitude,  $10^\circ$  longitude and 0.4 pressure scale height grid, with a lower boundary at  $2\mu\text{bar}$  (300 km above the 1 bar (B) level) and an upper boundary at 0.02 nbar.

### 2.2 Ionosphere model

The ionosphere model we employ is the same as that described in *Yates et al.* [2014] and *Yates et al.* [2018]. The model is separated into two parts: i) a vertical part describing the relative change of conductivity with altitude [*Grodent et al.*, 2001]; and ii) a horizontal part, that scales the vertical conductivity profiles such that the height-integrated Pedersen conductance  $\Sigma_P$  is equal to the fixed values which we prescribe. The only difference between this ionospheric model and that in *Yates et al.* [2018] is that here we have day-night variation in  $\Sigma_P$ . In this 3D model we have four fixed conductance regions:

1. polar regions ( $|\theta| > 74^\circ$ ) with  $\Sigma_P = 0.2$  mho [*Isbell et al.*, 1984];
2. auroral region ( $|\theta| = 60 - 74^\circ$ ) with  $\Sigma_P = 0.5$  mho [*Nichols*, 2011; *Yates et al.*, 2014];
3. day-side low latitude region ( $-60^\circ \leq \theta \leq 60^\circ$ ) with  $\Sigma_P = 0.0275$  mho [*Hill*, 1980];
4. night-side low latitude region ( $-60^\circ \leq \theta \leq 60^\circ$ ) with  $\Sigma_P = 0.0$  mho.

The conductance in the night-side low latitude (region 4 above) region is set to zero. The conductivity model employed in this study basically consists of conductances due to solar EUV radiation (region 3) and enhancements due to particle precipitation in the high-latitude regions (regions 1 and 2). Solar EUV does not reach the night-side ionosphere and so the conductance at low-latitudes depends on the lifetime of the ionospheric species and whether low-latitude particle precipitation is present. For simplicity, we assume that there is no low-latitude particle precipitation and that the lifetime of ionospheric species is small enough so that there is zero conductance on the night-side. This assumption does not influence the atmosphere as such as is investigated in this study. A future study will incorporate a more realistic night-side ionospheric conductance.

### 2.3 Magnetosphere model

We use the same magnetosphere model described in *Smith and Aylward* [2009]; *Yates et al.* [2012, 2014]; *Yates et al.* [2018] which is based on the works of *Nichols and Cowley* [2004]; *Cowley et al.* [2005] and *Cowley et al.* [2007]. The model is axisymmet-

167 ric, aligned with Jupiter’s rotation axis and solves for the magnetospheric plasma angular  
 168 velocity. Additionally, it allows for the magnetic mapping between the magnetosphere  
 169 and ionosphere. This mapping is achieved by assuming that surfaces of constant flux func-  
 170 tion form shells of magnetic field lines with common magnetospheric equatorial radial  
 171 distances  $\rho_e$  and ionospheric co-latitude  $\theta_i$ . As such, one can equate the ionospheric flux  
 172 function  $F_i(\theta_i)$  with its magnetospheric equivalent  $F_e(\rho_e)$  (magnetic flux integrated be-  
 173 tween a given  $\rho_e$  and infinity) giving

$$F_i(\theta_i) = B_J R_i^2 \sin^2 \theta_i = F_e(\rho_e). \quad (1)$$

174 Where  $B_J = 426\,400$  nT [Connerney *et al.*, 1998] and is the equatorial magnetic field  
 175 strength at the planet’s surface.  $R_i$  is the ionospheric radius which for this study we set  
 176 to  $R_J$ .  $F_e(\rho_e)$  (and the corresponding equatorial magnetic field) are taken from *Nichols*  
 177 *and Cowley* [2004].

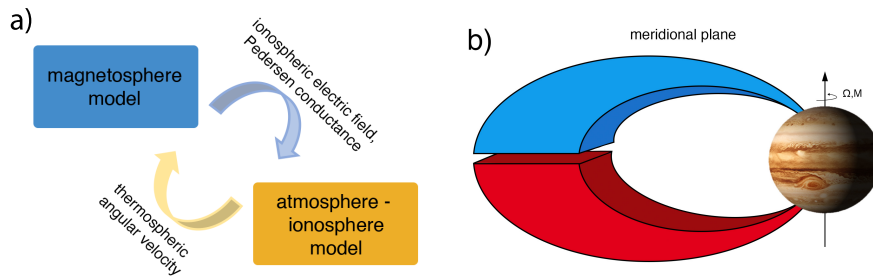
#### 178 2.4 Coupled Magnetosphere-Ionosphere-Thermosphere model

179 Our three model components are coupled as shown in Fig. 1a. The atmospheric  
 180 module solves the time-dependent Navier-Stokes equations before passing an “effective”  
 181 thermospheric angular velocity  $\Omega_T$  to the magnetosphere module.  $\Omega_T$  is the weighted  
 182 average of all the horizontal winds and is the thermospheric neutral velocity that the  
 183 magnetosphere sees (see *Smith and Aylward* [2008, 2009] for details on how this is cal-  
 184 culated). The magnetosphere module solves for the steady-state magnetospheric plasma  
 185 angular velocity  $\Omega_M$  using the Hill-Pontius equation [*Hill*, 1979; *Pontius and Hill*, 1982;  
 186 *Pontius*, 1997] which balances the torque between the outward diffusion of iogenic plasma  
 187 in the magnetosphere and the  $\mathbf{J} \times \mathbf{B}$  force associated with magnetosphere-ionosphere cur-  
 188 rents [*Yates et al.*, 2012]. These two angular velocities combined with the height-integrated  
 189 Pedersen conductance from the ionosphere module enable us to self-consistently determine  
 190 the MI coupling currents and the resultant heating of the atmosphere due to the magne-  
 191 toospheric interaction. The full details on how these modules are coupled together can be  
 192 found in *Smith and Aylward* [2009]; *Yates et al.* [2012, 2014] and *Ray et al.* [2015]. In this  
 193 new 3D model the northern and southern magnetospheric hemispheres are solved sepa-  
 194 rately and then combined in the thermosphere module. We also only couple the noon lo-  
 195 cal time / longitude gridpoints of the thermosphere to our magnetosphere model and then  
 196 impose the resulting magnetospheric currents to the other longitudes of the thermosphere.  
 197 The noon local time coupling is schematically shown in Fig. 1b. The limitations of our  
 198 current approach are discussed below.

#### 202 2.5 Limitations of the current model

203 Given that this model is built on the previous models of *Smith and Aylward* [e.g.  
 204 2009]; *Yates et al.* [e.g. 2014] it also shares some of their limitations. We begin by briefly  
 205 describing some of the common limitations before discussing limitations which are particu-  
 206 lar to the current model.

- 207 1. Using fixed Pedersen conductances in the auroral region ( $\pm 60 - 74^\circ$  latitude). Works  
 208 by *Yates et al.* [2012, 2014] have shown that using a fixed Pedersen conductance,  
 209 instead of a variable one, in this region does not significantly alter the local ther-  
 210 mospheric dynamics and heating if we consider perfect coupling between the iono-  
 211 sphere and magnetosphere i.e. there are no field-aligned potential (FAP) drops. We  
 212 also employ a fixed, albeit smaller, Pedersen conductance polewards of the auroral  
 213 region. The ionosphere and precipitating particles in this region are only recently  
 214 being investigated by Jupiter’s polar orbiting Juno spacecraft which will undoubt-  
 215 edly shed light on the conditions in this relatively unexplored region of Jupiter’s



199 **Figure 1.** a) Diagram representing our coupled magnetosphere-ionosphere-thermosphere model. b)  
 200 Schematic showing the separate magnetosphere models for each magnetic hemisphere which couple to  
 201 the thermosphere model.

216 upper atmosphere and high-latitude magnetosphere. The day- and night-side equa-  
 217 torial regions have little, if any, MI coupling there so having a fixed conductivity in  
 218 these regions will not influence the coupled model.

- 219 2. Using a fixed magnetospheric plasma angular velocity profile mapping to Jupiter's  
 220 outer magnetosphere ( $\pm 74 - 80^\circ$  latitude) and polar cap ( $> \pm 80^\circ$  latitude). We  
 221 employ fixed estimates of Jupiter's magnetospheric plasma flow (based on works  
 222 by *Isbell et al.* [1984] and *Cowley et al.* [2005]) in these regions due to the limited  
 223 amount of measurements taken in Jupiter's distant magnetosphere. Recent work  
 224 by *Johnson et al.* [2017] has shown that there is a strongly sub-corotating ( $\sim <$   
 225  $20\%$ ) ion flow region possibly mapping to the distant magnetosphere. Therefore,  
 226 we continue to use these fixed flow assumptions to allow comparison with older  
 227 models and until further observations are available.
- 228 3. No field-aligned potential (FAP) development. In this work we do not allow for  
 229 the development of FAP drops resulting in the decoupling between the ionospheric  
 230 and magnetospheric flows - we assume perfect MI coupling. Work by *Ray et al.*  
 231 [2015] was the first to include FAPs in a MIT coupling model and found that neu-  
 232 tral temperatures and flows were changed by a few percent when compared to the  
 233 same MIT model without FAPs. The variation in the Pedersen conductance due to  
 234 its self-consistent formulation was found to have a greater influence on the thermo-  
 235 sphere.

236 Our model uses a full 3D thermospheric GCM and ideally this would be coupled  
 237 to a full 3D magnetohydrodynamic (MHD) magnetosphere model but this is currently too  
 238 computationally expensive to carry out any feasible studies. Simplifications of the MIT  
 239 system therefore need to be made to allow for reasonable computation times. As discussed  
 240 in section 2.4, our approach is to couple our axisymmetric magnetosphere model [based  
 241 on *Yates et al.*, 2014] to the noon local time (LT) slice of the thermosphere assuming that  
 242 the magnetosphere is aligned with Jupiter's rotation axis. We solve for the northern and  
 243 southern magnetosphere separately before combining the results in the thermosphere. We  
 244 then project and impose the magnetospheric output at all other LT/longitudes. The result  
 245 is a 3D GCM coupled to a magnetosphere with no zonal variation. This is not physically  
 246 realistic as Jupiter's magnetosphere shows much local time variation [e.g. *Khurana*, 2001;  
 247 *Ray et al.*, 2014; *Comnerney et al.*, 2018]. However, we do believe this model to be a suit-  
 248 able intermediate step-towards a more comprehensive and self-consistent 3D MIT coupled  
 249 model. It allows us to investigate the influence of gradually increasing the complexity of  
 250 the coupled system.

## 2.6 Angular velocity profiles

In this study we present two simulations, one using a two-dimensional atmosphere model [Yates *et al.*, 2014] and the other using the new three-dimensional atmospheric GCM described above. Both simulations employ a magnetodisc size of  $65 R_J$  with all parameters kept equal. The simulations have been run for 500 rotations and have achieved steady-state.

The normalized thermospheric and magnetospheric angular velocities discussed above are plotted as a function of atmospheric latitude in Fig. 2. Solid lines show the new 3D output and dashed lines show 2D output from Yates *et al.* [2014] for comparison. Thermospheric angular velocities are shown in blue and purple lines while magnetospheric angular velocities are shown in red and yellow lines. Magnetospheric angular velocities essentially remain unchanged between the 2D and 3D models due to the similarities in the magnetosphere model. The thermospheric angular velocities however differ, particularly for latitudes polewards of  $75^\circ$ . These polar regions sub-corotate to a larger degree in the 3D simulation compared to the 2D one until  $\sim 86^\circ$  where 3D velocities increase to  $\sim 70\%$  of corotation. This highlights the difference between using an axisymmetric atmospheric GCM and a full 3D one which will be discussed in more detail below.

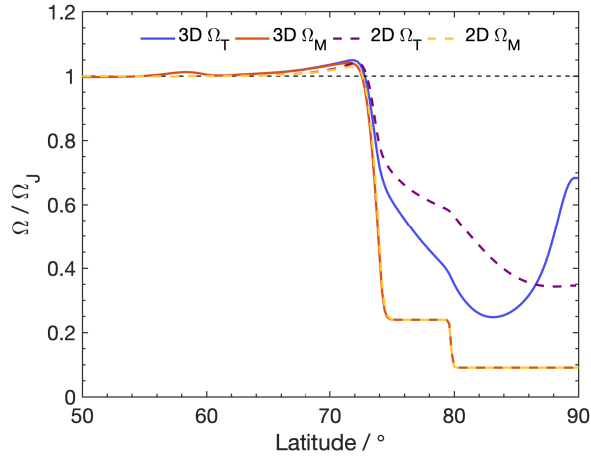


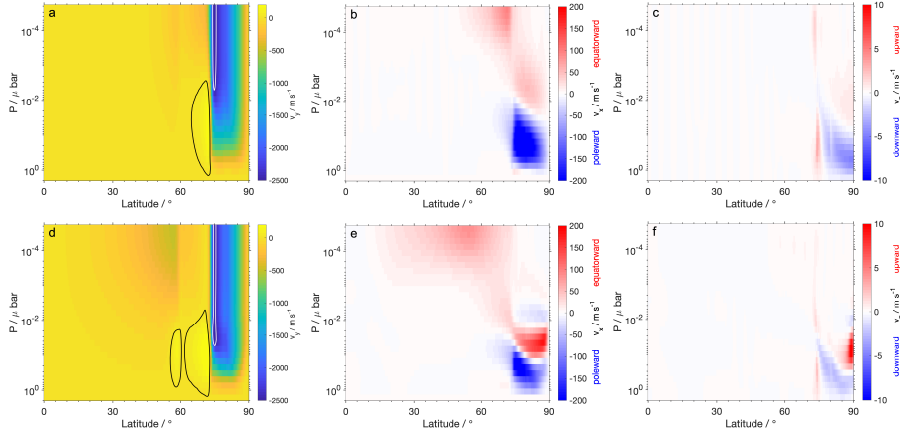
**Figure 2.** 3D (solid lines) and 2D (dashed lines) thermospheric (blue and purple lines) and magnetospheric (red and yellow lines) angular velocity profiles as a function of latitude.

## 3 Simulation results: 3D and 2D comparison

### 3.1 Atmospheric dynamics

Fig. 3 compares neutral wind velocities between our new 3D (Figs. 3d-f) simulation and an equivalent 2D northern hemisphere (Figs. 3a-c) steady-state simulation [Yates *et al.*, 2014]. Figs. 3 a, d show the zonal (east-west) winds in the corotation frame as a function of pressure and latitude. Figs. 3 b, e show meridional (north-south) winds and Figs. 3 c, f show vertical (up-down) winds respectively as a function of pressure and latitude. The structure of the neutral winds remains almost unchanged between our 2D and 3D simulations. The 3D zonal winds show strong sub-corotating (blue colors) jets in the polar regions (latitudes  $>75^\circ$ ) and also weaker sub-corotating jets at mid-latitudes. Super-corotating (black contour) jets are also seen at low altitudes in each simulation. In our 2D simulation the winds are more corotational (sub-corotating and super-corotating to a lesser

282 degree). The meridional winds consist of strong poleward flows (blue) at high latitudes  
 283 and low altitudes. At high altitudes most of the flows are equatorward. The main differ-  
 284 ences between our 2D and 3D simulations is that the mid-altitude, high-latitude equa-  
 285 torward 3D flow is much stronger ( $\sim 2\times$ ) than the 2D model meaning that mid-altitude  
 286 winds can transport heat equatorwards. Vertical winds are very similar in both simula-  
 287 tions but the upward winds in the poles are much stronger ( $\sim 2.75\times$ ) in the 3D simulation.  
 288 The faster 3D winds lead to the averaged thermospheric angular velocity profiles shown  
 289 in Fig. 2. In particular, the angular velocity profile polewards of  $\sim 85^\circ$  shows that neutral  
 290 winds are significantly faster than in the 2D simulation and approach  $\sim 0.7\Omega_J$  at the poles.  
 291 In the 3D simulation, eastwards (corotational) fictitious (Coriolis and curvature) forces  
 292 are unopposed at low altitudes beyond  $75^\circ$ , this accelerates the neutrals towards corota-  
 293 tion and given that this low altitude region has a stronger weighting in the  $\Omega_T$  calculations  
 294 due to its higher ionospheric conductances [see *Smith and Aylward, 2009*] compared to alti-  
 295 tudes above, the integrated average  $\Omega_T$  profile shows much faster winds near the poles.  
 296 The large flow shears near the poles require faster vertical winds in order to maintain hy-  
 297 drostatic equilibrium.



298 **Figure 3.** 2D (top row) and 3D (bottom row) neutral winds as a function of pressure and latitude. a)  
 299 and d) show azimuthal (east-west) velocities in the corotating frame. Black contours enclose regions of  
 300 super-corotation greater than  $25 \text{ m s}^{-1}$  and white contours enclose regions of sub-corotation slower than  
 301  $-2500 \text{ m s}^{-1}$ . b) and e) show meridional (north-south) velocities where equatorward (poleward) flows are posi-  
 302 tive (negative). c) and f) show vertical velocities with upwards (downwards) flows being positive (negative).

303 Figs. 4a, c show neutral temperature as a function of pressure and latitude for the  
 304 2D and 3D simulation respectively. Fig. 4b shows the 3D temperature as a function of lat-  
 305 itude and local time (LT) at the top pressure level of the model (0.02 nbar). The arrows  
 306 indicate the direction of the horizontal winds. In addition, Fig. 4d shows the vertical ther-  
 307 mal structure for our 2D (dashed colored lines) and 3D (solid colored lines) simulations  
 308 at various latitudes (see figure legend) compared with the Galileo probe measurements  
 309 shown in black line.

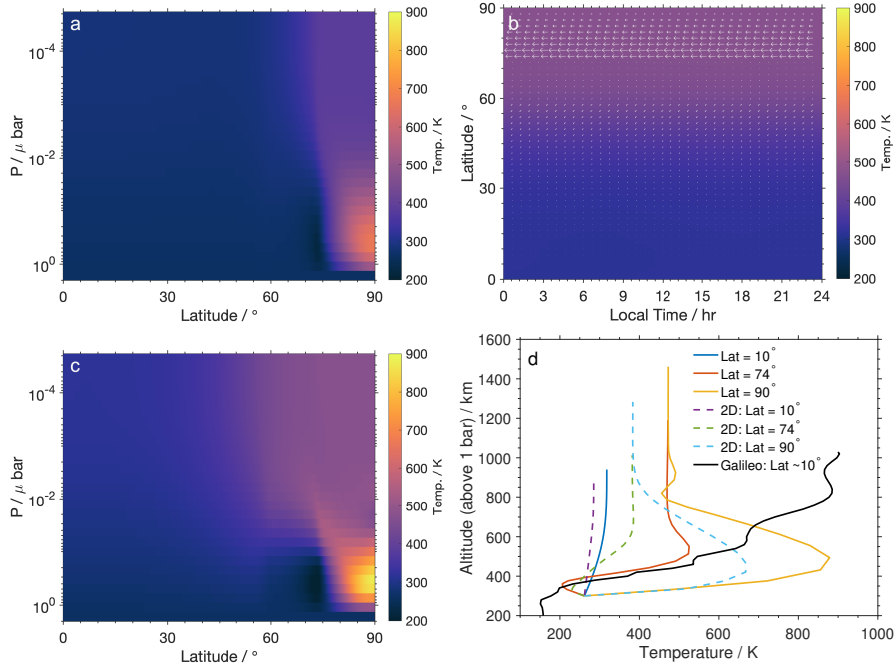
310 From Figs. 4a and c we see that the latitudinal and vertical structure remains rela-  
 311 tively unchanged between our 2D and 3D models i.e. hot polar regions with a cold equa-  
 312 tor. The polar hotspots arise from the advection of Joule heating and ion drag energy  
 313 near the model auroral zone ( $\sim 74^\circ$ ) towards the poles by strong meridional winds [e.g.  
 314 *Smith and Aylward, 2008, 2009; Tao et al., 2009; Yates et al., 2012; Ray et al., 2015*]. These  
 315 rapid poleward winds also lead to up-welling of neutrals just equatorward of the auroral



316 zone which are cooled adiabatically creating a relatively cold spot. Adiabatic heating from  
 317 down-welling at the poles and vertical advection also contribute to the polar hotspots.  
 318 The cold equatorial regions result from the lack of low-latitude heat sources (in the cur-  
 319 rent model setup) and the ‘ion drag fridge’ effect discussed by *Smith et al.* [2007]; *Smith*  
 320 *and Aylward* [2008] which gives rise to the strong low-altitude poleward flows discussed  
 321 above. This effect confines heat from the magnetospheric interaction into the polar regions  
 322 while essentially cooling the mid-to-low latitudes. Fig. 4b shows the hot pole and cold  
 323 equator. In particular, it shows the minimal effect, compared to other heat sources, of solar  
 324 radiation in heating the Jovian upper thermosphere.

325 The only difference between the two simulations is that the 3D atmosphere is hotter  
 326 than the 2D one, at mid and high latitudes. In fact, the maximum temperature in the  
 327 3D simulation is  $\sim 200$  K hotter than the 2D one (see also Fig. 4d). The increase in tem-  
 328 perature is due to a number of factors including, but not limited to, the faster wind speeds  
 329 being able to redistribute more heat (including to mid and low latitudes), the increased  
 330 heating rates (compared to 2D) at polar mid-altitudes and auroral latitudes, and additional  
 331 zonal advection terms – albeit this is local time dependent.

332 In Fig. 4d we see the improvement achieved with this new 3D simulation (compared  
 333 to the 2D one) in increasing the temperature of Jupiter’s upper atmosphere. Despite this,  
 334 there is still a large discrepancy at equatorial latitudes. This suggests that the current as-  
 335 sumptions employed here and in much of the recent literature are still inadequate and that  
 336 these need to be removed and/or amended to explain the observations.



337 **Figure 4.** 2D (a) and 3D (c) neutral temperature as a function of pressure and latitude. b) shows the 3D  
 338 temperature distribution as a function of local time (LT) and latitude. The arrows show the horizontal winds  
 339 with arrow length representing their speed. d) shows the vertical thermal structure for the 2D (dashed colored lines)  
 340 and 3D (solid colored lines) simulation at latitudes of  $10^\circ$ ,  $74^\circ$ ,  $90^\circ$  and that measured with the Galileo  
 341 probe (black line) [*Seiff et al.*, 1998].

### 3.2 Coupling currents and auroral emission

The currents responsible for coupling Jupiter's atmosphere and magnetosphere can be approximated to a three-current circuit: i) the Pedersen current in the ionosphere, ii) the radial current in the magnetosphere, and iii) the field-aligned current (FAC) completing the circuit. The Pedersen current is directed equatorwards and Eq. 2 gives the azimuthally-integrated Pedersen current  $I_P(\theta_i)$  [e.g. Cowley *et al.*, 2007; Smith and Aylward, 2009] representing the total current in each hemisphere.

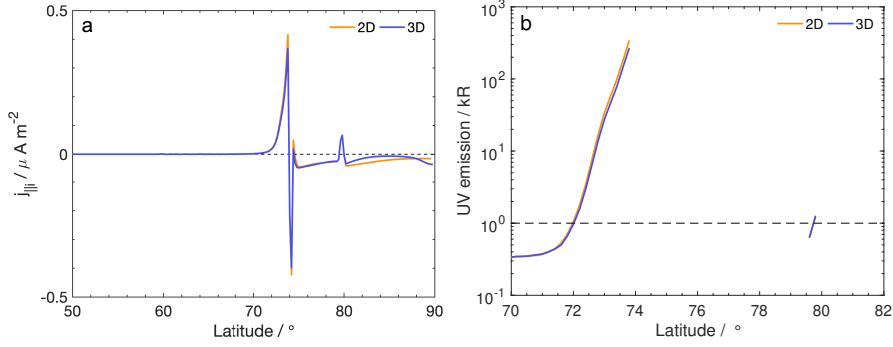
$$I_P(\theta_i) = 2\pi\rho_i\Sigma_P E_\theta, \quad (2)$$

where  $\rho_i$  is the perpendicular distance to the planet's magnetic/rotation axis, and  $E_\theta = B_i\rho_i(\Omega_T - \Omega_M)$  is the meridional electric field in the rest frame of the neutrals.  $B_i (= 2B_J)$  is the magnitude of the radial ionospheric magnetic field. Radial currents are directed radially outwards in the magnetosphere and FACs connect the ionosphere to magnetosphere. FACs are responsible for angular momentum and energy transfer between the ionosphere and magnetosphere. The FAC density at the ionosphere is given by

$$j_{||i}(\theta_i) = -\frac{1}{2\pi R_i^2 \sin\theta_i} \frac{dI_P}{d\theta_i}. \quad (3)$$

Fig. 5a compares the FAC density profiles in the 3D simulation (blue line) with the 2D simulation (orange line). Fig. 5b shows the corresponding brightness of the UV auroral emission associated with these FACs. Auroral emissions are calculated from the precipitating electron energy flux assuming that  $1 \text{ mW m}^{-2} = 10 \text{ kR}$  as described by Yates *et al.* [2014] [based on the works of Knight, 1973; Lundin and Sandahl, 1978; Cowley *et al.*, 2007] in order to allow for comparison. However, it is worth noting that recent Juno observations [Ebert *et al.*, 2019] have found that the above relationship between downward energy flux and auroral emission is not always true across the auroral region, or would require a deeper understanding of Jupiter electron acceleration region

The FAC density profiles show regions of strong upward FACs maximizing at  $74^\circ$ . Upward FACs mean downward propagating electrons which collide with atmospheric neutrals and result in UV emission. These upward FACs therefore correspond to the large peaks in auroral emission shown in Fig. 5b which represent the main auroral oval in our coupled MIT model. The regions of upward FAC are immediately followed by strong downward FACs indicating the return current. With the present model, no emission is expected in this region. Even further poleward, our model has another region of upward FACs and corresponding UV emission but with much smaller magnitude than that of the main oval. This region corresponds to the boundary between our model's outer magnetosphere (or cushion region) and the polar cap (open field region). The magnetospheric flows in this region are not well constrained by observations so the currents and emissions are susceptible to the values we prescribe for plasma flow and ionospheric conductances here. The maximum upward FAC in the 3D simulation is  $\sim 90\%$  that of the 2D simulation. This difference is caused by the shear between the neutral and plasma angular velocities being larger around  $\sim 74^\circ$  latitude in the 2D simulation than in the 3D one because of the 3D neutral winds sub-corotating to a larger degree in this region (see Fig. 2). The corresponding maximum auroral emissions amount to UV brightnesses of  $\sim 270 \text{ kR}$  for our 3D simulation and  $\sim 340 \text{ kR}$  for the 2D one with total integrated powers of  $\sim 2 \text{ TW}$  and  $\sim 2.5 \text{ TW}$  respectively. These emissions are of similar order-of-magnitude to observations and the integrated powers are comparable to recent observations taken using the Hubble Space Telescope (HST) [e.g. 1-3 TW in Grodent *et al.*, 2018], the Hisaki space telescope [e.g.  $\sim 1.3 \text{ TW}$  up to  $\sim 11 \text{ TW}$  Tao *et al.*, 2018], and the UVS instrument [Gladstone *et al.*, 2017a] onboard the Juno spacecraft [e.g. 2-3 TW in Gladstone *et al.*, 2017b].



387 **Figure 5.** Ionospheric field-aligned current density (a) and auroral ultraviolet (UV) emission (b) is shown  
 388 as a function of latitude. 2D and 3D current/emission are represented by the orange and blue lines respec-  
 389 tively. The dashed line in (b) shows the limit of detectability of the Hubble Space Telescope (HST).

### 390 3.3 Atmospheric energetics

391 We also examine the energy transferred from Jupiter’s deep rotation to its upper  
 392 atmosphere and magnetosphere. The power per unit area available due to Jupiter’s rota-  
 393 tion is given by  $P$ , this can be subdivided into the power used to accelerate sub-corotating  
 394 plasma within Jupiter’s magnetosphere  $P_M$  and the power dissipated within Jupiter’s upper  
 395 atmosphere consisting of Joule heating  $P_{JH}$  and ion drag  $P_{ID}$ .

$$P = \Omega_J \tau, \quad (4)$$

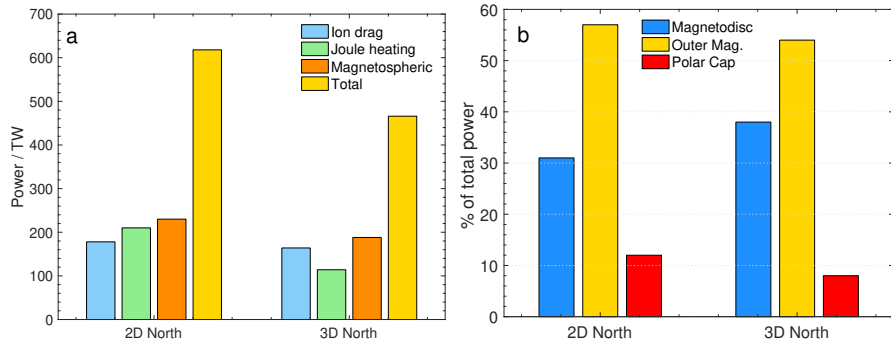
$$P_{JH} = (\Omega_T - \Omega_M) \tau, \quad (5)$$

$$P_{ID} = (\Omega_J - \Omega_T) \tau, \quad (6)$$

$$P_M = \Omega_M \tau, \quad (6)$$

396 where  $\tau = \rho_i i_P B_i$  is the torque exerted by the  $\mathbf{J} \times \mathbf{B}$  force per unit area of the ionosphere.  
 397  $i_P = I_P / (2\pi \rho_i)$  and is the Pedersen current density.

403 Fig. 6a shows the integrated ion drag (light blue), Joule heating (light green), mag-  
 404 netospheric (orange) and total (gold) power per hemisphere for the 2D simulation (north-  
 405 ern hemisphere) along with the northern hemisphere in the 3D simulation. Immediately  
 406 obvious is that the powers in the 2D simulation are larger than each 3D hemisphere. Ion  
 407 drag, Joule heating and magnetospheric powers are respectively  $\sim 1.06\times$ ,  $\sim 1.8\times$  and  $\sim 1.2\times$   
 408 larger in the 2D simulation than the 3D. The differences between the 3D and 2D simu-  
 409 lations are primarily due to the difference in neutral angular velocity between the two.  
 410 As shown in Figs. 2, 3a and 3d, the neutral winds between  $73\text{--}86^\circ$  latitude sub-corotate  
 411 to a much larger degree in the 3D simulation leading to smaller Pedersen currents (and  
 412 torques) in the ionosphere. This large region of sub-corotating neutral flow maps to re-  
 413 gions of the magnetosphere whose flows are prescribed in our model ( for details see  
 414 section 2.5 or *Yates et al. [2012]* ) suggesting that these changes are purely due to atmo-  
 415 spheric effects and the added momentum and energy terms in the 3D simulation. Fig. 6b  
 416 shows the fraction of power in atmospheric regions mapping to the magnetodisc ( $55.4\text{--}$   
 417  $74.2^\circ$  latitude shown in blue), outer magnetosphere ( $74.2\text{--}79.8^\circ$  latitude shown in gold)  
 418 and polar cap ( $79.8\text{--}90^\circ$  latitude shown in red). The fraction of power used in the outer  
 419 magnetosphere is similar for both 2D and 3D simulations. The differences lie in the power  
 420 used in the magnetodisc and polar cap regions where the 3D simulation uses  $\sim 7\%$  more  
 421 power in the magnetodisc and  $\sim 5\%$  less power in the polar cap. From Fig. 6b we see that



398 **Figure 6.** a) shows integrated ion drag (light blue), Joule heating (light green), magnetospheric (orange)  
 399 and total (gold) power per hemisphere for the 2D model and the northern hemisphere of the 3D model. b)  
 400 shows the fraction of total integrated power mapping to the magnetodisc (55.4 - 74.2° latitude shown in blue),  
 401 outer magnetosphere (74.2 - 79.8° latitude shown in gold) and polar cap (79.8 - 90° latitude shown in red)  
 402 regions of the magnetosphere.

422 approximately 60 – 70% of power extracted from Jupiter’s rotation is consumed within  
 423 atmospheric regions where we prescribe the plasma flows. In order to understand how  
 424 Jupiter’s atmosphere is heated we must gain better understanding of the plasma flows in  
 425 the high-latitude ionosphere which map to the distant magnetosphere.

## 426 4 Discussion

### 427 4.1 Comparison with observations

#### 428 4.1.1 Neutral temperatures

429 There are many in situ observations of Jupiter’s magnetosphere. On the other hand,  
 430 Jupiter’s atmosphere has only one set of in situ observations by NASA’s Galileo Probe  
 431 (see black line in Fig. 4d and/or *Seiff et al.* [1998]). All other observations of Jupiter’s at-  
 432 mosphere are remote (space- or Earth-based telescopes). Temperatures of Jupiter’s upper  
 433 atmosphere can be inferred remotely from auroral observations at infrared (IR) and ul-  
 434 traviolet (UV) wavelengths [e.g. *Yelle et al.*, 1996; *Lam et al.*, 1997; *Stallard et al.*, 2002;  
 435 *Raynaud et al.*, 2004; *Lystrup et al.*, 2008; *Adriani et al.*, 2017; *Moore et al.*, 2017; *Johnson*  
 436 *et al.*, 2018; *Kita et al.*, 2018; *Migliorini et al.*, 2019]. Using IR emission from the iono-  
 437 spheric  $H_3^+$  ion, Jupiter’s thermospheric temperature is observed to range from ~400 K  
 438 at 300 km (above the 1 bar level) and increasing to between ~900 K and ~1400 K at  
 439 altitudes  $\geq 700$  km, with larger temperatures located at higher latitudes [e.g. *Moore et al.*,  
 440 2017; *Johnson et al.*, 2018; *Migliorini et al.*, 2019].

441 Comparison of our model neutral temperatures to those observed can be split into  
 442 two regions:

- 443 1. The polar thermosphere ( $\geq 74^\circ$ ): Here, our model achieved its maximum temper-  
 444 ature of 878 K at low polar altitudes (~500 km). Our model temperatures then  
 445 decrease with increasing altitude to ~450 K. This is contrary to expectations and  
 446 available observations. This temperature inversion is likely caused by the lack of  
 447 (or weak) energy sources at high altitudes within our model. The heat in this re-  
 448 gion is transported towards the equator by the high altitude equatorward winds. The  
 449 higher model temperatures in this polar region are comparable to the lower limit of

450 the observed high-latitude temperatures but at higher altitudes our model tempera-  
 451 tures are at most 50% of those observed.

- 452 2. The mid-to-low latitude thermosphere ( $<74^\circ$ ): The high-altitude temperature max-  
 453 imums vary from  $\sim 320$  K at the equator to  $\sim 480$  K at  $70^\circ$ . These maximums are  
 454 approximately a factor-of-two times smaller than the mid-to-low latitude tem-  
 455 peratures derived by *O'Donoghue et al.* [2016] at altitudes between 600 km and  
 456 1000 km. At low altitudes these temperatures have an average of  $\sim 290$  K with a  
 457 base of 260 K at the lower boundary (equivalent to 300 km above the 1 bar level).  
 458 These temperatures are  $\sim 100 - 200$  K smaller than those determined at 300 km by  
 459 *Migliorini et al.* [2019]. Compared to the Galileo Probe measurements, our equato-  
 460 rial model temperatures are similar only at altitudes lower than 400 km; at higher  
 461 altitudes our equatorial temperatures are  $\sim 100 - 600$  K smaller than measured.

462 The differences between the model temperatures and observations act to highlight  
 463 that there is still much work to be done in being able to reproduce the observations. Other  
 464 sources of heat, such as wave heating [*Tao et al.*, 2009; *Müller-Wodarg et al.*, 2019], need  
 465 to be included the model as well as a better understanding of the distant magnetospheric  
 466 plasma flows.

#### 467 4.1.2 Neutral winds

468 In addition to estimating thermospheric neutral temperatures, Jupiter's auroral IR  
 469 emission can be used to determine the line-of-sight velocity of  $\text{H}_3^+$  ions (Jupiter's main  
 470 ionospheric constituent) using the Doppler shift technique [e.g. *Stallard et al.*, 2001; *Chaufray*  
 471 *et al.*, 2011; *Johnson et al.*, 2017]. The works of *Stallard* and *Johnson* find regions where  
 472 the ionosphere is super-corotating between  $\sim 0.5 - 1$  km  $\text{s}^{-1}$  and regions where it is sub-  
 473 corotating between  $\sim 1 - 2$  km  $\text{s}^{-1}$ . *Chaufray et al.* [2011] however only found ionospheric  
 474 winds sub-corotating at  $\sim 3$  km  $\text{s}^{-1}$ . Additionally, *Chaufray et al.*, estimated neutral wind  
 475 velocities in Jupiter's thermosphere using IR emissions from  $\text{H}_2$ ; these were found to be  
 476 of order  $\sim 1$  km  $\text{s}^{-1}$  suggesting that the neutral thermosphere rotates faster than the iono-  
 477 sphere. The authors do note that more simultaneous neutral and ion wind measurements  
 478 are needed to fully understand the system.

479 Our new 3D model obtains both super- and sub-corotating neutral winds and ion/plasma  
 480 angular velocities. The neutral zonal winds achieve velocities between  $\sim 0.25$  km  $\text{s}^{-1}$  (super-  
 481 corotating) and  $\sim -2.7$  km  $\text{s}^{-1}$  (sub-corotating). We do not calculate ionospheric ion winds  
 482 using the ion momentum equation but instead calculate the plasma angular velocity (using  
 483 the Hill-Pontius equation described in section 2.4) within the magnetosphere and assume  
 484 that the ionospheric plasma angular velocity is the same. In order to use this method, the  
 485 magnetosphere interacts with an 'effective' neutral thermosphere and therefore an 'effec-  
 486 tive' neutral angular velocity  $\Omega_T$  which is dependent on both the zonal and meridional  
 487 neutral winds. The plasma angular velocity up to the auroral region  $\sim 74^\circ$  tracks  $\Omega_T$  very  
 488 well albeit being a little smaller. Our model neutral and plasma velocities are comparable  
 489 to those in the above observational studies up to the auroral oval region. Poleward of this  
 490 region, our plasma flows are prescribed to rotate at a small fraction of Jupiter's rotation  
 491 velocity as is shown in Fig. 2. The polar region neutral flows are strongly influenced by  
 492 these prescribed flows and should be interpreted with a degree of scepticism. However, we  
 493 note that the line-of-sight velocity of  $\text{H}_3^+$  ions observed by *Johnson et al.* [2017] in their  
 494 UV-dark region shows flows which are near stationary ( $<20\%$  of  $\Omega_J$ ). If we assume that  
 495 the UV-dark region applies to a "polar cap" type region then these observations add cred-  
 496 ence to our use of small plasma velocities. Nevertheless, more observations of Jupiter's  
 497 polar ionosphere and outer magnetosphere are needed to further constrain the ionospheric  
 498 flows and NASA's Juno [*Bolton et al.*, 2017] can shed some light on this poorly under-  
 499 stood region.

## 4.2 Comparison with other Jovian 3D models

There are a few 3D Jovian upper atmospheric models which investigate Jupiter's MIT coupling (JIM and JTGCM). These models do not self-consistently couple the upper atmosphere to the magnetosphere but instead impose electric and magnetic fields, and MI coupling parameterizations onto the atmospheric model. They do however include detailed atmospheric chemistry and therefore include a somewhat realistic ionosphere. In contrast, the new model described in section 2 includes MIT coupling self-consistently in addition to solving the atmospheric neutral momentum and energy equations. It however, includes only a simplified conductivity parameterization representing Jupiter's ionosphere. The differences in the ionospheric components of these models result in different values of Pedersen conductances which is important in MIT coupling [e.g. *Ray et al.*, 2015]. The JIM [*Millward et al.*, 2002] model conductances are comparable ( $1 - 3\times$ ) to those used in this study but conductances in JTGCM [*Bougher et al.*, 2005] are  $\sim 10\times$  higher than those employed here. Furthermore, we assume that our magnetic field model is rotationally-aligned and axisymmetric, contrary to the magnetic field models employed in JIM (offset tilted dipole [*Acuna et al.*, 1983]) and JTGCM (VIP4 [*Connerney et al.*, 1998]). We therefore perform only simple comparisons between this new model and previous Jovian 3D MIT models. We note that this new model, as described herein, is midway in its development to include self-consistent 3D MIT coupling.

With regards to neutral temperature, our model is generally colder than both JIM and JTGCM with the exception being in the low-altitude polar regions where our models have comparable temperatures. JIM's atmospheric temperature increases from 400 K at the models lower boundary to 1200 K at its upper boundary and is heated primarily by Joule heating and auroral particle precipitation. It is worth noting that while the JIM model did reach a quasi-dynamical equilibrium state it did not achieve thermal equilibrium during its model runs. JTGCM includes ion drag, particle precipitation and Joule heating but their Joule heating parameterization requires being down-scaled to 15% in order to reproduce equatorial temperature profiles comparable to those observed by the Galileo Probe. JTGCM's high-latitude temperatures reach  $\sim 1100$  K in the southern polar region and  $\sim 900$  K in the northern due to asymmetries in the VIP4 magnetic field model.

Zonal thermospheric neutral velocities were found to be of order  $\sim 0.5$  km  $s^{-1}$  in the JIM model [e.g. *Millward et al.*, 2005] compared to  $\sim 1.6$  km  $s^{-1}$  and  $\sim 0.6$  km  $s^{-1}$  respectively in JTGCMs southern and northern auroral ovals [e.g. *Majeed et al.*, 2016]. These result from ion winds of  $\sim 1$  km  $s^{-1}$  in JIM and  $\sim 3.5$  km  $s^{-1}$  in JTGCM (note that ion winds are imposed in JTGCM). The zonal winds in our new model are typically stronger (more subcorotating) than both JIM and JTGCM, reaching sub-corotating values of  $\sim 2.7$  km  $s^{-1}$ . Our model also includes a region equatorward of the auroral oval where the neutral atmosphere super-corotates with speeds up to  $\sim 0.25$  km  $s^{-1}$  resulting from the Coriolis force and the strong ( $\sim 0.2 - 0.3$  km  $s^{-1}$ ) low altitude poleward winds. Above the peak conducting region, our meridional flows switch to being equatorward and with similar speed. These equatorward flows slow down to only a few m  $s^{-1}$  at the equator. The meridional winds in JTGCM and JIM are stronger than in the model presented herein and reach poleward speeds up to  $\sim 0.6$  km  $s^{-1}$  and equatorward speeds of  $\sim 0.25$  km  $s^{-1}$ . As discussed above, JTGCM employs the VIP4 magnetic field model which causes considerable asymmetry in heating and neutral flows. As such, JTGCM also obtains strong ( $\sim 0.1 - 0.2$  km  $s^{-1}$ ) equatorward flows even at low southern latitudes which allows for the redistribution of heat from the auroral region.

## 5 Summary and conclusions

Jupiter's upper atmosphere is  $\sim 700$  K hotter than predicted based on solar EUV heating alone. The interaction with Jupiter's strong and dynamic magnetosphere is thought to play a vital role in heating its upper atmosphere to its observed temperatures. However,

551 to date no coupled magnetosphere-ionosphere-thermosphere model has been able to self-  
 552 consistently reproduce Jupiter’s thermospheric temperatures without imposing particular  
 553 plasma flows, large Pedersen conductances inconsistent with modelling/predictions, and/or  
 554 including a low-latitude heat source such as acoustic wave breaking or small-scale Joule  
 555 heating generated by fluctuating electric fields. We present a new model of Jupiter’s MIT  
 556 coupled system that couples a three-dimensional atmospheric general circulation model to  
 557 an axisymmetric magnetosphere model. This new model is an intermediate step towards  
 558 the development of a self-consistently coupled 3D atmosphere-magnetosphere model. We  
 559 compare this new model to its two-dimensional predecessor, available observations and  
 560 other 3D Jovian upper atmosphere models.

561 Compared to the 2D simulations of *Yates et al.* [2014], the new model has a mean  
 562 temperature that is  $\sim 60$  K hotter, with a maximum temperature that is  $\sim 200$  K hotter in  
 563 the polar regions. Zonal and poleward neutral winds were found to be comparable in both  
 564 simulations while the equatorward winds are twice as strong ( $\sim 190$  m s $^{-1}$ ) in the new  
 565 3D simulation resulting in more energy transport from high to low latitudes. 3D vertical  
 566 winds were also found to be 2-3 $\times$  stronger in the upward direction and half as strong in  
 567 the downward direction. The velocity shear between the neutrals and plasma is larger in  
 568 the 2D simulation between  $74 - 86^\circ$  leading to larger MI coupling currents, powers, and  
 569 UV emission. Our 3D model is still in development and is not yet fully comparable to  
 570 the other 3D Jovian thermosphere models available. However, our model is converging  
 571 towards the results found in the JIM and JTGC models and unlike these models it also  
 572 includes self-consistent coupling between the ionosphere and magnetosphere. Our model  
 573 also compares reasonably well with some ionospheric wind observations and its predicted  
 574 total UV power is of the same order of magnitude as those determined from HST obser-  
 575 vations. The neutral temperatures in the auroral and polar regions are comparable to the  
 576 lower range of observed temperatures while the models equatorial temperatures are still a  
 577 few 100 K colder than observed.

578 The axisymmetric rotationally-aligned magnetosphere model that we employ in  
 579 this study results in a small (few degrees latitude) circular region of interaction between  
 580 Jupiter’s magnetosphere and atmosphere centred on  $74^\circ$  latitude. In actuality, Jupiter’s  
 581 magnetic field is tilted with respect to its rotation axis and has very complex structure  
 582 [e.g. *Connerney et al.*, 2018]. Furthermore, observations of Jupiter’s auroral emission -  
 583 a ‘visible’ manifestation of the MI interaction - show that this interaction region is any-  
 584 thing but small and circular; in fact, it is highly asymmetric within and between each  
 585 hemisphere [e.g. *Connerney et al.*, 2017]. Such a complex asymmetric interaction region  
 586 would lead to different neutral flow and heating structures which cannot be simulated with  
 587 the current model setup. The JIM and JTGC models, while not self-consistently cou-  
 588 pling the atmosphere and magnetosphere, do employ more realistic magnetic field mod-  
 589 els at the planet which is one of the main reasons that their findings are different from  
 590 those presented above. The next step in the development of the presented model is to in-  
 591 clude a more realistic magnetic field model [e.g. *Connerney et al.*, 2018] including real-  
 592 istic mapping from the magnetosphere to the ionosphere and local time variation, a more  
 593 detailed ionosphere model [e.g. *Blelly et al.*, 2019], and parameterizations allowing for the  
 594 incorporation of atmospheric waves [e.g. *Tao et al.*, 2009; *Müller-Wodarg et al.*, 2019].  
 595 This model will be the most realistic three-dimensional representation of Jupiter’s coupled  
 596 magnetosphere-atmosphere system.

### 597 Acknowledgments

598 J. N. Y. was supported by a European Space Agency research fellowship. L. C. R. ac-  
 599 knowledges the STFC Consolidated Grant ST/R000816/1. N. A. was supported by the  
 600 UK STFC Consolidated Grant (UCL/MSSL Solar and Planetary Physics, ST/N000722/1).  
 601 The authors acknowledge the International Space Science Institute (ISSI) for their sup-  
 602 port of the ‘Coordinated Numerical Modeling of the Global Jovian and Saturnian Sys-

603 tems' team. The Galileo Probe observations are available from the Planetary Data System  
 604 (<http://pds.nasa.gov/>) and are peer reviewed. The simulation output used in this study is  
 605 available at <https://figshare.com/s/9c49fecbc77634b83cd> but confidential until manuscript  
 606 is accepted. The authors would like to thank both referees for their useful suggestions.

## 607 References

- 608 Achilleos, N., S. Miller, J. Tennyson, A. D. Aylward, I. Mueller-Wodarg, and D. Rees  
 609 (1998), JIM: A time-dependent, three-dimensional model of Jupiter's thermo-  
 610 sphere and ionosphere, *Journal of Geophysical Research*, *103*, 20,089–20,112, doi:  
 611 10.1029/98JE00947.
- 612 Achilleos, N., S. Miller, R. Prangé, G. Millward, and M. K. Dougherty (2001), A dynami-  
 613 cal model of Jupiter's auroral electrojet, *New Journal of Physics*, *3*, 3, doi:10.1088/1367-  
 614 2630/3/1/303.
- 615 Acuna, M. H., K. W. Behannon, and J. E. P. Connerney (1983), *Jupiter's magnetic field*  
 616 *and magnetosphere*, pp. 1–50.
- 617 Adriani, A., A. Mura, M. L. Moriconi, B. M. Dinelli, F. Fabiano, F. Altieri, G. Sindoni,  
 618 S. J. Bolton, J. E. P. Connerney, and S. K. Atreya (2017), Preliminary JIRAM results  
 619 from Juno polar observations: 2. Analysis of the Jupiter southern H<sub>3</sub><sup>+</sup> emissions and  
 620 comparison with the north aurora, *Geophysical Research Letters*, *44*(10), 4633–4640,  
 621 doi:10.1002/2017GL072905.
- 622 Bletly, P.-L., A. Marchaudon, M. Indurain, O. Witasse, J. Amaya, B. Chide, N. Andr  ,  
 623 V. G  not, A. Goutenoir, and M. Bouchemit (2019), Transplanet: A web service dedi-  
 624 cated to modeling of planetary ionospheres, *Planetary and Space Science*, *169*, 35 – 44,  
 625 doi:<https://doi.org/10.1016/j.pss.2019.02.008>.
- 626 Bolton, S. J., J. Lunine, D. Stevenson, J. E. P. Connerney, S. Levin, T. C. Owen, F. Bage-  
 627 nal, D. Gautier, A. P. Ingersoll, G. S. Orton, T. Guillot, W. Hubbard, J. Bloxham,  
 628 A. Coradini, S. K. Stephens, P. Mokashi, R. Thorne, and R. Thorpe (2017), The Juno  
 629 Mission, *Space Science Reviews*, *213*, 5–37, doi:10.1007/s11214-017-0429-6.
- 630 Bougher, S. W., J. H. Waite, T. Majeed, and G. R. Gladstone (2005), Jupiter Thermo-  
 631 spheric General Circulation Model (JTGCM): Global structure and dynamics driven  
 632 by auroral and Joule heating, *Journal of Geophysical Research (Planets)*, *110*, E04008,  
 633 doi:10.1029/2003JE002230.
- 634 Chaufray, J.-Y., T. K. Greathouse, G. R. Gladstone, J. H. Waite, J.-P. Maillard, T. Majeed,  
 635 S. W. Bougher, E. Lellouch, and P. Drossart (2011), Spectro-imaging observations of  
 636 Jupiters 2  $\mu\text{m}$  auroral emission. II: Thermospheric winds, *Icarus*, *211*, 1233–1241, doi:  
 637 10.1016/j.icarus.2010.11.021.
- 638 Connerney, J. E. P., M. H. Acu  a, N. F. Ness, and T. Satoh (1998), New models of  
 639 Jupiter's magnetic field constrained by the Io flux tube footprint, *Journal of Geophys-  
 640 ical Research*, *103*, 11,929–11,940, doi:10.1029/97JA03726.
- 641 Connerney, J. E. P., A. Adriani, F. Allegrini, F. Bagenal, S. J. Bolton, B. Bonfond,  
 642 S. W. H. Cowley, J.-C. Gerard, G. R. Gladstone, D. Grodent, G. Hospodarsky, J. L.  
 643 Jorgensen, W. S. Kurth, S. M. Levin, B. Mauk, D. J. McComas, A. Mura, C. Parani-  
 644 cas, E. J. Smith, R. M. Thorne, P. Valek, and J. Waite (2017), Jupiter's magnetosphere  
 645 and aurorae observed by the Juno spacecraft during its first polar orbits, *Science*, *356*,  
 646 826–832, doi:10.1126/science.aam5928.
- 647 Connerney, J. E. P., S. Kotsiaros, R. J. Oliverson, J. R. Espley, J. L. Joergensen, P. S. Jo-  
 648 ergensen, J. M. G. Merayo, M. Herceg, J. Bloxham, K. M. Moore, S. J. Bolton, and  
 649 S. M. Levin (2018), A new model of jupiter's magnetic field from juno's first nine or-  
 650 bits, *Geophysical Research Letters*, *45*(6), 2590–2596, doi:10.1002/2018GL077312.
- 651 Cowley, S. W. H., I. I. Alexeev, E. S. Belenkaya, E. J. Bunce, C. E. Cottis, V. V. Kale-  
 652 gaev, J. D. Nichols, R. Prang  , and F. J. Wilson (2005), A simple axisymmetric model  
 653 of magnetosphere-ionosphere coupling currents in Jupiter's polar ionosphere, *Journal of*  
 654 *Geophysical Research*, *110*, 11,209–11,226, doi:10.1029/2005JA011237.



- 655 Cowley, S. W. H., J. D. Nichols, and D. J. Andrews (2007), Modulation of Jupiter's  
 656 plasma flow, polar currents, and auroral precipitation by solar wind-induced compres-  
 657 sions and expansions of the magnetosphere: a simple theoretical model, *Ann. Geophys.*,  
 658 25, 1433–1463.
- 659 Ebert, R. W., T. K. Greathouse, G. Clark, F. Allegrini, F. Bagenal, S. J. Bolton, J. E. P.  
 660 Connerney, G. R. Gladstone, M. Imai, V. Hue, W. S. Kurth, S. Levin, P. Louarn, B. H.  
 661 Mauk, D. J. McComas, C. Paranicas, J. R. Szalay, M. F. Thomsen, P. W. Valek, and  
 662 R. J. Wilson (2019), Comparing Electron Energetics and UV Brightness in Jupiter's  
 663 Northern Polar Region During Juno Perijove 5, *Geophysical Research Letters*, 46, 19–  
 664 27, doi:10.1029/2018GL081129.
- 665 Gladstone, G. R., S. C. Persyn, J. S. Eterno, B. C. Walther, D. C. Slater, M. W. Davis,  
 666 M. H. Versteeg, K. B. Persson, M. K. Young, G. J. Dirks, A. O. Sawka, J. Tumlinson,  
 667 H. Sykes, J. Beshears, C. L. Rhoad, J. P. Cravens, G. S. Winters, R. A. Klar, W. Lock-  
 668 hart, B. M. Piepgrass, T. K. Greathouse, B. J. Trantham, P. M. Wilcox, M. W. Jackson,  
 669 O. H. W. Siegmund, J. V. Vallerga, R. Raffanti, A. Martin, J.-C. Gérard, D. C. Gro-  
 670 dent, B. Bonfond, B. Marquet, and F. Denis (2017a), The Ultraviolet Spectrograph on  
 671 NASA's Juno Mission, *Space Science Reviews*, 213, 447–473, doi:10.1007/s11214-014-  
 672 0040-z.
- 673 Gladstone, G. R., M. H. Versteeg, T. K. Greathouse, V. Hue, M. W. Davis, J.-C. Gérard,  
 674 D. C. Grodent, B. Bonfond, J. D. Nichols, R. J. Wilson, G. B. Hospodarsky, S. J.  
 675 Bolton, S. M. Levin, J. E. P. Connerney, A. Adriani, W. S. Kurth, B. H. Mauk,  
 676 P. Valek, D. J. McComas, G. S. Orton, and F. Bagenal (2017b), Juno-UVS approach  
 677 observations of Jupiter's auroras, *Geophysical Research Letters*, 44, 7668–7675, doi:  
 678 10.1002/2017GL073377.
- 679 Grodent, D., J. H. Waite, and J. Gérard (2001), A self-consistent model of the Jovian  
 680 auroral thermal structure, *Journal of Geophysical Research*, 106, 12,933–12,952, doi:  
 681 10.1029/2000JA900129.
- 682 Grodent, D., B. Bonfond, Z. Yao, J.-C. Gérard, A. Radioti, M. Dumont, B. Palmaerts,  
 683 A. Adriani, S. V. Badman, E. J. Bunce, J. T. Clarke, J. E. P. Connerney, G. R. Glad-  
 684 stone, T. Greathouse, T. Kimura, W. S. Kurth, B. H. Mauk, D. J. McComas, J. D.  
 685 Nichols, G. S. Orton, L. Roth, J. Saur, and P. Valek (2018), Jupiter's Aurora Observed  
 686 With HST During Juno Orbits 3 to 7, *Journal of Geophysical Research (Space Physics)*,  
 687 123, 3299–3319, doi:10.1002/2017JA025046.
- 688 Hickey, M. P., R. L. Walterscheid, and G. Schubert (2000), Gravity Wave Heating and  
 689 Cooling in Jupiter's Thermosphere, *Icarus*, 148, 266–281, doi:10.1006/icar.2000.6472.
- 690 Hill, T. W. (1979), Inertial limit on corotation, *Journal of Geophysical Research*, 84,  
 691 6554–6558, doi:10.1029/JA084iA11p06554.
- 692 Hill, T. W. (1980), Corotation lag in Jupiter's magnetosphere - Comparison of observation  
 693 and theory, *Science*, 207, 301, doi:10.1126/science.207.4428.301.
- 694 Isbell, J., A. J. Dessler, and J. H. Waite, Jr. (1984), Magnetospheric energization by inter-  
 695 action between planetary spin and the solar wind, *Journal of Geophysical Research*, 89,  
 696 10,716–10,722, doi:10.1029/JA089iA12p10716.
- 697 Johnson, R. E., T. S. Stallard, H. Melin, J. D. Nichols, and S. W. H. Cowley (2017),  
 698 Jupiter's polar ionospheric flows: High resolution mapping of spectral intensity and  
 699 line-of-sight velocity of h<sup>3+</sup> ions, *Journal of Geophysical Research: Space Physics*,  
 700 122(7), 7599–7618, doi:10.1002/2017JA024176.
- 701 Johnson, R. E., H. Melin, T. S. Stallard, C. Tao, J. D. Nichols, and M. N. Chowdhury  
 702 (2018), Mapping h<sup>3+</sup> temperatures in jupiter's northern auroral ionosphere using  
 703 vlt-crites, *Journal of Geophysical Research: Space Physics*, 123(7), 5990–6008, doi:  
 704 10.1029/2018JA025511.
- 705 Khurana, K. K. (2001), Influence of solar wind on Jupiter's magnetosphere deduced from  
 706 currents in the equatorial plane, *Journal of Geophysical Research*, 106, 25,999–26,016,  
 707 doi:10.1029/2000JA000352.

- 708 Kita, H., S. Fujisawa, C. Tao, M. Kagitani, T. Sakanoi, and Y. Kasaba (2018), Horizontal  
709 and vertical structures of Jovian infrared aurora: Observation using Subaru IRCS with  
710 adaptive optics, *Icarus*, *313*, 93–106, doi:10.1016/j.icarus.2018.05.002.
- 711 Knight, S. (1973), Parallel electric fields, *Planetary and Space Science*, *21*, 741–750, doi:  
712 10.1016/0032-0633(73)90093-7.
- 713 Lam, H. A., N. Achilleos, S. Miller, J. Tennyson, L. M. Trafton, T. R. Geballe, and G. E.  
714 Ballester (1997), A Baseline Spectroscopic Study of the Infrared Auroras of Jupiter,  
715 *Icarus*, *127*, 379–393, doi:10.1006/icar.1997.5698.
- 716 Lundin, R., and I. Sandahl (1978), Some characteristics of the parallel electric field ac-  
717 celeration of electrons over discrete auroral arcs as observed from two rocket flights,  
718 in *European Sounding Rocket, Balloon and Related Research, with Emphasis on Experi-*  
719 *ments at High Latitudes, ESA Special Publication*, vol. 135, edited by T. Halvorsen and  
720 B. Battrock, pp. 125–136.
- 721 Lystrup, M. B., S. Miller, N. Dello Russo, R. J. Vervack, Jr., and T. Stallard (2008), First  
722 Vertical Ion Density Profile in Jupiter’s Auroral Atmosphere: Direct Observations using  
723 the Keck II Telescope, *Astrophysical Journal*, *677*, 790–797, doi:10.1086/529509.
- 724 Majeed, T., J. H. Waite, S. W. Bougher, and G. R. Gladstone (2005), Processes of equa-  
725 torial thermal structure at Jupiter: An analysis of the Galileo temperature profile with  
726 a three-dimensional model, *Journal of Geophysical Research (Planets)*, *110*, E12007,  
727 doi:10.1029/2004JE002351.
- 728 Majeed, T., J. H. Waite, S. W. Bougher, and G. R. Gladstone (2009), Processes of auroral  
729 thermal structure at Jupiter: Analysis of multispectral temperature observations with  
730 the Jupiter Thermosphere General Circulation Model, *Journal of Geophysical Research*  
731 *(Planets)*, *114*, E07005, doi:10.1029/2008JE003194.
- 732 Majeed, T., S. W. Bougher, A. J. Ridley, J. H. Waite, G. R. Gladstone, and J. M. Bell  
733 (2016), Global response of the upper thermospheric winds to large ion drifts in the  
734 Jovian ovals, *Journal of Geophysical Research (Space Physics)*, *121*, 4647–4667, doi:  
735 10.1002/2015JA021328.
- 736 Matcheva, K. I., and D. F. Strobel (1999), Heating of Jupiter’s Thermosphere by Dissipa-  
737 tion of Gravity Waves Due to Molecular Viscosity and Heat Conduction, *Icarus*, *140*,  
738 328–340, doi:10.1006/icar.1999.6151.
- 739 Migliorini, A., B. M. Dinelli, M. L. Moriconi, F. Altieri, A. Adriani, A. Mura, J. E. P.  
740 Connerney, S. K. Atreya, G. Piccioni, and F. Tosi (2019),  $H_3^+$  characteristics in the  
741 Jupiter atmosphere as observed at limb with Juno/JIRAM, *Icarus*, *329*, 132–139, doi:  
742 10.1016/j.icarus.2019.04.003.
- 743 Miller, S., N. Achilleos, G. E. Ballester, T. R. Geballe, R. D. Joseph, R. Prangé,  
744 D. Rego, T. Stallard, J. Tennyson, L. M. Trafton, and J. H. Waite, Jr. (2000), The  
745 role of  $H_3^+$  in planetary atmospheres, in *Astronomy, physics and chemistry of  $H_3^+$* ,  
746 *Royal Society of London Philosophical Transactions Series A*, vol. 358, p. 2485, doi:  
747 10.1098/rsta.2000.0662.
- 748 Millward, G., S. Miller, T. Stallard, A. D. Aylward, and N. Achilleos (2002), On the Dy-  
749 namics of the Jovian Ionosphere and Thermosphere III. The Modelling of Auroral Con-  
750 ductivity, *Icarus*, *160*, 95–107, doi:10.1006/icar.2002.6951.
- 751 Millward, G., S. Miller, T. Stallard, N. Achilleos, and A. D. Aylward (2005), On the dy-  
752 namics of the jovian ionosphere and thermosphere.. IV. Ion-neutral coupling, *Icarus*,  
753 *173*, 200–211, doi:10.1016/j.icarus.2004.07.027.
- 754 Moore, L., J. O’Donoghue, H. Melin, T. Stallard, C. Tao, B. Zieger, J. Clarke, M. F.  
755 Vogt, T. Bhakyaipbul, and M. Opher (2017), Variability of Jupiter’s IR  $H_3^+$  auro-  
756 rae during Juno approach, *Geophysical Research Letters*, *44*(10), 4513–4522, doi:  
757 10.1002/2017GL073156.
- 758 Müller-Wodarg, I. C. F., M. Mendillo, R. V. Yelle, and A. D. Aylward (2006), A global  
759 circulation model of Saturn’s thermosphere, *Planetary and Space Science*, *180*, 147–160,  
760 doi:10.1016/j.icarus.2005.09.002.

- 761 Müller-Wodarg, I. C. F., T. T. Koskinen, L. Moore, J. Serigano, R. V. Yelle, S. Hörst,  
762 J. H. Waite, and M. Mendillo (2019), Atmospheric Waves and Their Possible Effect on  
763 the Thermal Structure of Saturn’s Thermosphere, *Geophysical Research Letters*, *46*(5),  
764 2372–2380, doi:10.1029/2018GL081124.
- 765 Nichols, J., and S. Cowley (2004), Magnetosphere-ionosphere coupling currents in  
766 Jupiter’s middle magnetosphere: effect of precipitation-induced enhancement of the  
767 ionospheric Pedersen conductivity, *Ann. Geophys.*, *22*, 1799–1827.
- 768 Nichols, J. D. (2011), Magnetosphere-ionosphere coupling in Jupiter’s middle mag-  
769 netosphere: Computations including a self-consistent current sheet magnetic  
770 field model, *Journal of Geophysical Research (Space Physics)*, *116*, A10232, doi:  
771 10.1029/2011JA016922.
- 772 O’Donoghue, J., L. Moore, T. S. Stallard, and H. Melin (2016), Heating of Jupiter’s  
773 upper atmosphere above the Great Red Spot, *Nature*, *536*(7615), 190–192, doi:  
774 10.1038/nature18940.
- 775 Pontius, D. H. (1997), Radial mass transport and rotational dynamics, *Journal of Geophys-*  
776 *ical Research*, *102*, 7137–7150, doi:10.1029/97JA00289.
- 777 Pontius, D. H., Jr., and T. W. Hill (1982), Departure from corotation of the Io plasma  
778 torus - Local plasma production, *Geophysical Research Letters*, *9*, 1321–1324, doi:  
779 10.1029/GL009i012p01321.
- 780 Ray, L. C., N. A. Achilleos, M. F. Vogt, and J. N. Yates (2014), Local time variations in  
781 Jupiter’s magnetosphere-ionosphere coupling system, *Journal of Geophysical Research*  
782 *(Space Physics)*, *119*, 4740–4751, doi:10.1002/2014JA019941.
- 783 Ray, L. C., N. A. Achilleos, and J. N. Yates (2015), The effect of including field-aligned  
784 potentials in the coupling between Jupiter’s thermosphere, ionosphere, and magne-  
785 tosphere, *Journal of Geophysical Research (Space Physics)*, *120*, 6987–7005, doi:  
786 10.1002/2015JA021319.
- 787 Raynaud, E., E. Lellouch, J.-P. Maillard, G. R. Gladstone, J. H. Waite, B. Bézard,  
788 P. Drossart, and T. Fouchet (2004), Spectro-imaging observations of Jupiter’s 2- $\mu\text{m}$   
789 auroral emission. I.  $\text{H}_3^+$  distribution and temperature, *Icarus*, *171*, 133–152, doi:  
790 10.1016/j.icarus.2004.04.020.
- 791 Schubert, G., M. P. Hickey, and R. L. Walterscheid (2003), Heating of Jupiter’s thermo-  
792 sphere by the dissipation of upward propagating acoustic waves, *Icarus*, *163*, 398–413,  
793 doi:10.1016/S0019-1035(03)00078-2.
- 794 Seiff, A., D. B. Kirk, T. C. D. Knight, R. E. Young, J. D. Mihalov, L. A. Young, F. S.  
795 Milos, G. Schubert, R. C. Blanchard, and D. Atkinson (1998), Thermal structure of  
796 Jupiter’s atmosphere near the edge of a 5- $\mu\text{m}$  hot spot in the north equatorial belt, *Jour-*  
797 *nal of Geophysical Research*, *103*, 22,857–22,890, doi:10.1029/98JE01766.
- 798 Smith, C. G. A., and A. D. Aylward (2008), Coupled rotational dynamics of Saturn’s ther-  
799 mosphere and magnetosphere: a thermospheric modelling study, *Ann. Geophys.*, *26*,  
800 1007–1027.
- 801 Smith, C. G. A., and A. D. Aylward (2009), Coupled rotational dynamics of Jupiter’s ther-  
802 mosphere and magnetosphere, *Ann. Geophys.*, *27*, 199–230.
- 803 Smith, C. G. A., S. Miller, and A. D. Aylward (2005), Magnetospheric energy inputs into  
804 the upper atmospheres of the giant planets, *Ann. Geophys.*, *23*, 1943–1947.
- 805 Smith, C. G. A., A. D. Aylward, G. H. Millward, S. Miller, and L. E. Moore (2007), An  
806 unexpected cooling effect in Saturn’s upper atmosphere, *Nature*, *445*, 399–401, doi:  
807 10.1038/nature05518.
- 808 Stallard, T., S. Miller, G. Millward, and R. D. Joseph (2001), On the Dynamics of the  
809 Jovian Ionosphere and Thermosphere. I. The Measurement of Ion Winds, *Icarus*, *154*,  
810 475–491, doi:10.1006/icar.2001.6681.
- 811 Stallard, T., S. Miller, G. Millward, and R. D. Joseph (2002), On the Dynamics of  
812 the Jovian Ionosphere and Thermosphere. II. The Measurement of  $\text{H}_3^+$  Vibrational  
813 Temperature, Column Density, and Total Emission, *Icarus*, *156*, 498–514, doi:  
814 10.1006/icar.2001.6793.

- 815 Strobel, D. F., and G. R. Smith (1973), On the temperature of the Jovian ther-  
 816 mosphere., *Journal of Atmospheric Sciences*, *30*, 718–725, doi:10.1175/1520-  
 817 0469(1973)030<0718:OTTOTJ>2.0.CO;2.
- 818 Tao, C., H. Fujiwara, and Y. Kasaba (2009), Neutral wind control of the Jovian  
 819 magnetosphere-ionosphere current system, *Journal of Geophysical Research*, *114*, 8307–  
 820 8323, doi:10.1029/2008JA013966.
- 821 Tao, C., H. Fujiwara, and Y. Kasaba (2010), Jovian magnetosphere-ionosphere current  
 822 system characterized by diurnal variation of ionospheric conductance, *Planetary and*  
 823 *Space Science*, *58*, 351–364, doi:10.1016/j.pss.2009.10.005.
- 824 Tao, C., Y. Miyoshi, N. Achilleos, and H. Kita (2014), Response of the Jovian ther-  
 825 mosphere to variations in solar EUV flux, *Journal of Geophysical Research (Space*  
 826 *Physics)*, *119*, 3664–3682, doi:10.1002/2013JA019411.
- 827 Tao, C., T. Kimura, F. Tsuchiya, G. Muirakami, K. Yoshioka, A. Yamazaki, S. V. Badman,  
 828 H. Misawa, H. Kita, Y. Kasaba, I. Yoshikawa, and M. Fujimoto (2018), Variation of  
 829 Jupiter’s Aurora Observed by Hisaki/EXCEED: 3. Volcanic Control of Jupiter’s Aurora,  
 830 *Geophysical Research Letters*, *45*(1), 71–79, doi:10.1002/2017GL075814.
- 831 Waite, J. H., T. E. Cravens, J. Kozyra, A. F. Nagy, S. K. Atreya, and R. H. Chen (1983),  
 832 Electron precipitation and related aeronomy of the Jovian thermosphere and ionosphere,  
 833 *Journal of Geophysical Research*, *88*, 6143–6163, doi:10.1029/JA088iA08p06143.
- 834 Yates, J. N., N. Achilleos, and P. Guio (2012), Influence of upstream solar wind  
 835 on thermospheric flows at Jupiter, *Planetary and Space Science*, *61*, 15–31, doi:  
 836 10.1016/j.pss.2011.08.007.
- 837 Yates, J. N., N. Achilleos, and P. Guio (2014), Response of the Jovian thermosphere to a  
 838 transient ‘pulse’ in solar wind pressure, *Planetary and Space Science*, *91*, 27–44, doi:  
 839 10.1016/j.pss.2013.11.009.
- 840 Yates, J. N., L. C. Ray, and N. Achilleos (2018), An initial study into the long-term influ-  
 841 ence of solar wind dynamic pressure on jupiter’s thermosphere, *Journal of Geophysical*  
 842 *Research: Space Physics*, doi:10.1029/2018JA025828.
- 843 Yelle, R. V., and S. Miller (2004), *Jupiter’s thermosphere and ionosphere*, pp. 185–218.
- 844 Yelle, R. V., L. A. Young, R. J. Vervack, R. Young, L. Pfister, and B. R. Sandel (1996),  
 845 Structure of Jupiter’s upper atmosphere: Predictions for Galileo, *Journal of Geophysical*  
 846 *Research*, *101*, 2149–2162, doi:10.1029/95JE03384.
- 847 Young, L. A., R. V. Yelle, R. Young, A. Seiff, and D. B. Kirk (1997), Gravity waves in  
 848 Jupiter’s thermosphere., *Science*, *276*, 108–111, doi:10.1126/science.276.5309.108.